Energy materials

Vertical Fe(OH)$_3$/Ni$_9$S$_8$ nanoarrays electrodeposited on stainless steel as binder-free electrocatalyst for highly efficient and stable oxygen evolution reaction

Xin Chen[1], Xinqiang Wang[1,2,*], Xiaojuan Zhang[1], Katam Srinivas[1], Dawei Liu[1], Xingchuan Zhao[1], Hesheng Yu[1], Bin Wang[1], Wanli Zhang[1], and Yuanfu Chen[1,3,*]

[1] *School of Electronic Science and Engineering, and State Key Laboratory of Electronic Thin Films and Integrated Devices, University of Electronic Science and Technology of China, Chengdu 610054, People's Republic of China*

[2] *Institute of Science and Technology for New Energy, Xi'an Technological University, Xi'an 710021, People's Republic of China*

[3] *Institute of Oxygen Supply, and College of Science, Tibet University, Lhasa 850000, People's Republic of China*

ABSTRACT

The widely acknowledged water splitting catalysis as an alternative to fossil fuel combustion becomes unproductive due to the involved sluggish oxygen evolution reaction (OER) kinetics. Therefore, it is extremely urgent and significant to develop an inexpensive OER catalyst with fast reaction dynamics, high efficiency and long-term stability. To address such issues, herein, for the first time, we present a novel vertical Fe(OH)$_3$/Ni$_9$S$_8$ nanoarrays electrocatalyst that can rapidly fabricated on etched stainless steel (ESS) via a facile and swift electrodeposition process. The Fe(OH)$_3$/Ni$_9$S$_8$/ESS exhibits excellent OER performance with ultra-low overpotential of 206 mV at 10 mA cm^{-2} (far better than RuO$_2$/ESS) and shows outstanding long-term stability. The terrific OER performance can be attributed to the integration of well-designed nanoarchitecture, and the coupling effect between Fe(OH)$_3$ and Ni$_9$S$_8$. The direct nanoarrays electrodeposition on highly conductive ESS substrate not only facilitate the rapid electron transfer for enhanced performance, but also improve the mechanical properties to ensure long-term stability. Additionally, the well-designed porous nanoarray guarantees abundant catalytically active sites exposure, facilitate the electrolyte penetration and promote the O$_2$ bubble release. Interestingly, the systematically fabricated Fe(OH)$_3$ outer layer can prevent the direct contact of Ni$_9$S$_8$ layer with alkaline electrolyte to avoid surface oxidation during catalysis. This work provides a systematic strategy to rationally design and facilely fabricate low-cost electrocatalysts with outstanding OER performance.

Introduction

The prosperity of human society relies heavily on fossil fuels, which are converted into carbon dioxide and released into the atmosphere in the process of utilization, thus leading to the greenhouse effect [1, 2]. Therefore, weakening or even completely replacing the current energy structure has become an inevitable problem. Water splitting, as a form of energy conversion without harmless byproduct, has attracted the attention of many research teams. However, the popularity of this new form of energy is hampered by complex four-electron process of oxygen evolution reaction (OER), a half reaction of water splitting [3, 4]. As commercial catalysts, Ru- and Ir-based materials have played a great role in promoting the sluggish OER process [5]. Yet, it is precisely because of their high cost the industrial scale applications have been limited.

Up to now, transition metal-based phosphides [6–10], borides [11, 12], nitrides [13–16], selenides [17–21], and sulfides [22–26], etc. showed excellent performance in accelerating the OER process. Among of them, nickel sulfide has been widely concerned because of its excellent electrical conductivity and high intrinsic activity. For instance, *Zhang* et al. [27]. prepared Ni-S/graphene heterostructure electrocatalyst, that requires an overpotential of 300 mV to afford OER at 10 mA cm^{-2}. Similarly, *Chen* et al. reported the superior OER activity (297 mV @ 11 mA cm^{-2}) of Ni-S nanosheet fabricated by hydrothermal method [28]. However, these electrocatalytic performances of nickel sulfide used in OER process are far from meeting the requirements of mass production and need to be improved urgently. In fact, the modification of the above sulfides and even most catalysts is mainly based on two points: morphology optimization and the electronic structure modulation [29, 30]. So far, quite a few research results emerge from zero-dimensional quantum dots to three-dimensional hybrid structures. For instance, *Mohanty* et al. successfully synthesized MoS$_2$ quantum dots, which possess outstanding OER performance (370 mV @ 10 mA cm^{-2} and 39 mV dec^{-1}) [31]. *Dai* and co-workers fabricated self-assembled Ni$_{0.7}$Co$_{0.3}$P nanoflower, which presented an enhanced performance for OER (230 mV @ 10 mA cm^{-2} and 78 mV dec^{-1}) [32]. Among the reported nanostructures with different morphologies,

the vertically aligned nanoarray structure with larger surface area and more exposed electrochemically active sites are of great significance to improve the electrochemical performance for OER [33, 34]. In addition, adjusting the electronic structure of the catalyst is another effective strategy for improving the electrocatalytic activity. For nickel-based sulfides, the addition of Ni/Fe-based hydroxides can significantly promote the catalytic activity of OER [35–37]. *Liu* synthesized a NiCo$_2$S$_4$/NiFe LDH interface by hydrothermal possess, wherein the electronic interactions between NiCo$_2$S$_4$ and NiFe LDH have been regulated to suppress the free energy of intermediate, thus enhancing the catalytic activity [37].

Based on the above analysis, it is significant to combine morphology optimization and regulate the electronic structure at the same time to obtain excellent catalytic performance of nickel sulfide, thus, a controllable two-step electrochemical deposition method for constructing a neoteric Fe(OH)$_3$/Ni$_9$S$_8$ nanoarrays on etched stainless steel was first developed as efficient and stable OER electrocatalyst. The advantages of particular structure are stated below: (1) The open vertical array of Fe(OH)$_3$/Ni$_9$S$_8$ nanosheets not only exposed a wealth of catalytic active sites, but also increased the opportunity for electrolyte solution to contact with catalytic active sites and oxygen release during OER process. (2) The interaction between Fe(OH)$_3$ and Ni$_9$S$_8$ creates a more favorable interface for the OER. (3) The outer layer of Fe(OH)$_3$ prevents the Ni$_9$S$_8$ layer from direct contact with the electrolyte and thus avoiding the additional Ni oxidation potential. (4) The self-supporting growth catalyst deposited on conductive substrate can avoid the covering of active sites by binder and thus further improve the OER performance. (5) The structure prepared by electrodeposition will make the active materials firmly attached on ESS, thus ensuring its durable performance. Therefore, under the condition of inheriting the above advantages, the Fe(OH)$_3$/Ni$_9$S$_8$/ESS has displayed ultra-low overpotential (206 mV @ 10 mA cm^{-2}), which outperforms the RuO$_2$/ESS (310 mV @ 10 mA cm^{-2}). This systematic study provides an inspiration for the design of low-cost and high efficiency catalysts for boosted OER performance.

Experimental section

Synthesis of Ni$_9$S$_8$/ESS

First of all, the stainless steel (SS) was cut into 3*2 cm^2 pieces, then washed with deionized water and alcohol for several times, and finally put it into 4 M HCl and etched for 25 min by ultrasonication. Subsequently, the etched stainless steel (ESS) was placed in an electric oven at 60 °C for 8 h prior to electrodeposition.

The typical synthesis of nickel sulfide on ESS substrates as follows. The electrolyte for the first electrodeposition includes 0.26 M thioacetamide (TAA) and 0.05 M nickel nitrate hexahydrate (Ni(NO$_3$)$_2$.6-H$_2$O). The deposition of precursor was executed under the DC stabilized power supply. During the electrodeposition process, carbon rod was used as anode and the ESS was used as cathode, and the potentiation deposition (5 V) was selected for 40 s. After the deposition, the surface of the electrode was washed with deionized water and dried at 60 °C in an electric oven.

Synthesis of Fe(OH)$_3$/Ni$_9$S$_8$/ESS

The electrode prepared above was used as the Cathode for the secondary deposition, and the electrolyte was replaced with 0.02 M ammonium ferrous sulfate [(NH$_4$)$_2$Fe(SO$_4$)$_2$], and the anode was still a carbon rod. Deposition in constant current mode (2 mA cm^{-2}) was used for 60 s, and then the surface of the electrode was washed with deionized water and dried in the 60 °C oven.

Synthesis of RuO$_2$/ESS

As a reference group, 2 mg cm^{-2} RuO$_2$ loaded ESS was prepared as follows; first, 5 mg of RuO$_2$ was dispersed in 750 μL of deionized water (DW), 100 μL of Nafion and 150 μL of alcohol, then ultrasonication was performed until the mixture was evenly distributed. Finally, the mixture was dropped onto ESS. Next, the sample prepared above is then left overnight in an electric oven at 60 °C (denoted as RuO$_2$/ESS).

Material characterizations

X-ray diffractometer (XRD) diffractometer was used to measure the composition and crystal phase of samples treated with different processes, which recorded on X'pert PRO PEP (Cu Ka) with 2θ from 10 to 80 degrees. Materials loaded on the substrate are identified by X-ray photoelectron spectroscopy (XPS, Thermo Scientific K-Alpha) mainly the valence and composition. The micromorphology of the prepared samples was obtained from scanning electron microscopy (SEM, ZEISS Gemini 300, OXFORD Xplore) and transmission electron microscopy (TEM, FEI Tecnai G2 F20, OXFORD X-max 80 T).

Measurements of electrocatalytic properties

The related OER performance tests were performed on a typical three-electrode electrochemical workstation. The sample to be tested served as the working electrode, saturated Hg/HgO electrode was served as the reference electrode, and a carbon rod was used as the counter electrode. Cyclic voltammetry (CV) was employed before the linear voltammetry scanning (LSV) between 0 and 0.8 V (vs. Hg/HgO) at a scan rate of 0.1 V s^{-1}. The LSV used to determine the OER performance curve, which is scanned in reverse direction (0.8–0 V vs. Hg/HgO) at a low scanning rate (2 mV s^{-1}). All potentials measured by electrochemical workstations have been corrected using the Nernst equation: $E_{RHE} = E_{Hg/HgO} + 0.923$ V. Finally, the overpotential is the potential at the reversible hydrogen electrode corresponding to 10 mA cm^{-2} in the LSV curve minus 1.23 V. The Tafel slope is calculated by Tafel formula based on LSV data. The impedance spectra of different samples were tested by setting the frequency in the range of 0.1 Hz–100 kHz at the voltage of 0.513 V vs. Hg/HgO. The cyclic voltammetry was obtained by scanning from 40 to 200 mV s^{-1} with 50 mV s^{-1} interval in the non-Faraday region (0.953–1.053 V vs. RHE). The long-term stability was determined by 12 h chronoamperometry test at a constant voltage of 1.44 V vs. RHE. The stability of the catalyst was tested after 500 cycles of voltammetry in 1 M KOH.

Results and discussion

Material characterization

The fabrication process of as-synthesized vertical nanoarrays is depicted in Fig. 1. In this method, the smooth surface of stainless steel (Fig.S1a, e, g) is modified for better deposition of the active material. After 30 min of acid etching, the surface of the stainless steel becomes rough and owns cracks and pits on its surface (Fig.S1b, f, h), which provides suitable surface conditions for the uniform deposition of the precursor. At the same time, it is worth mentioning that, compared with the untreated stainless steel, the overpotential and Tafel slope of the stainless steel after acid etching are greatly reduced (Fig.S4). Subsequently, Ni_9S_8 nanoarrays was formed on the ESS (Fig.S1c, i) after the first electrodeposition. Finally, Fe(II) ions in solution reacted with reduced oxygen and water to form $Fe(OH)_3$ at the surface of Ni_9S_8 nanoarrays to construct $Fe(OH)_3/Ni_9S_8$ composite catalyst on ESS (Fig.S1d, j) in the second electrochemical deposition process.

In addition, in the second deposition process, we took deposition time as the independent variable and 10 s interval as the time gradient. Through the test, we found that with the increase of deposition time, the catalytic performance also increased significantly and reached the maximum value at 40 s, so the later experimental tests were all based on the second 40 s.

The morphologies of as-papered samples were obtained by SEM. According to Fig. 2a and Fig. 2b, the vertically arranged nanoarrays grow uniformly on the surface of the ESS, and the morphology of the one and two-step deposition is basically the same with slightly differences, which indicates that the newly deposited species on the surface have no effect on the morphology. The remaining vertical open structure allows more open space for the catalyst to be in contact with the electrolyte, and thus facilitating charge transfer and mass transport. In order to clarify the elements contained in the secondary deposition products, the overall morphology EDS mapping (Fig. 2c) was carried out and the results showed that Fe, Ni, S and O were uniformly distributed on the microstructure surface. To indicate the composition of the growing material on the ESS matrix, the XRD tests were performed and the results are shown in Fig. S2a., All the XRD patterns show that the samples during different processes have the same three strong peaks of the austenite, which originated from the ESS substrate. And, it can be seen that after each electrodeposition, the sample displays a weaker peak than previous sample, which respectively indicates the generation of nickel sulfide and iron hydroxide. However, due to the strong inherent peak of stainless steel and the thin active material deposited on the SS surface (Fig. S2d), the phase peak of as-prepared catalyst is not prominent. Thus, we then use XPS to figure out the main form of elements in the surface of the samples. As shown in Fig.S2b, Ni, Fe, S and O elements all exist in the prepared $Fe(OH)_3/ESS$ catalyst, which is consistent with the EDS result. The 2p region of nickel divides (Fig. 3a) into two regions, including Ni $2p_{1/2}$ and $2p_{3/2}$. The three peaks at 854.98 (Ni^{2+}), 855.2 (Ni^{3+}), and 859.8 eV (satellite peak) belong to the Ni $2p_{3/2}$ region, and the binding energies located at 871.3 (Ni^{2+}), 873.2 (Ni^{3+}), and 877.8 eV (satellite peak) are ascribed to Ni $2p_{1/2}$ region. These results about the peak of nickel accord with the characteristic peaks of Ni_9S_8 species [38–40]. It is noteworthy that the Ni 2p peak of the $Fe(OH)_3/Ni_9S_8/ESS$ shifts in a negative direction compared with the Ni_9S_8/ESS (Fig.S2c) without the addition of the second step of iron hydroxide (Ni $2p_{3/2}$ peaks

Figure 1 Schematic illustration of synthesis procedure for $Fe(OH)_3/Ni_9S_8/$ ESS.
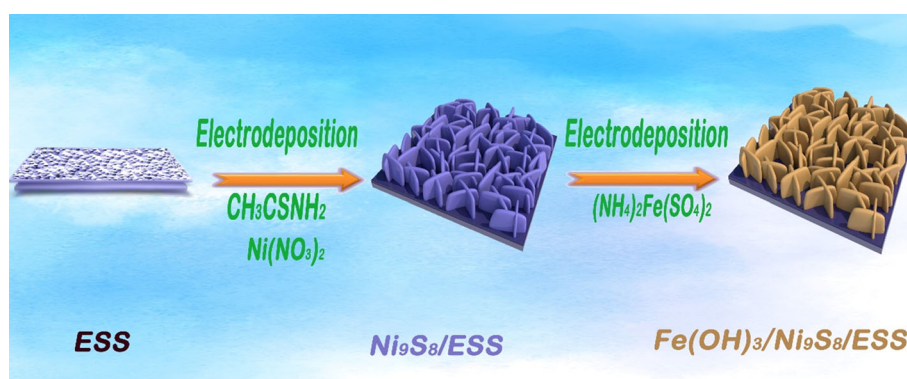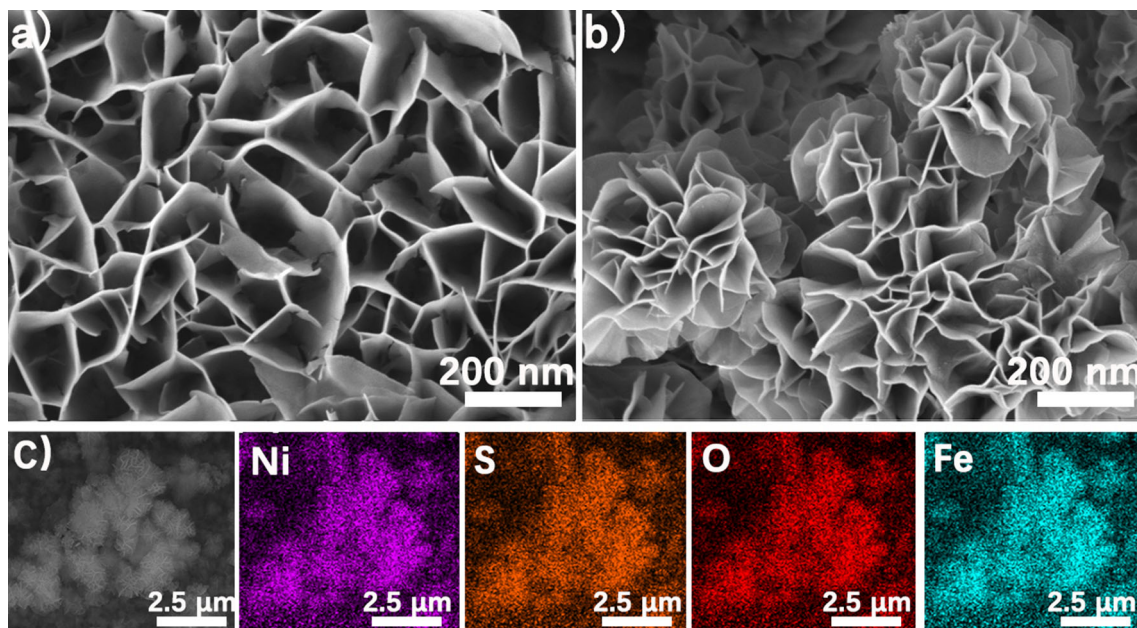
Figure 2 SEM images of **a** Ni₉S₈/ESS **b** and Fe(OH)₃/Ni₉S₈/ESS. **c** Overall morphology and EDS elemental mappings of Fe(OH)₃/Ni₉S₈/ESS.

Figure 3 **a** Ni 2p, **b** Fe 2p, **c** S 2p and **d** O 1 s core-level XPS spectra of Fe(OH)₃/Ni₉S₈/ESS.
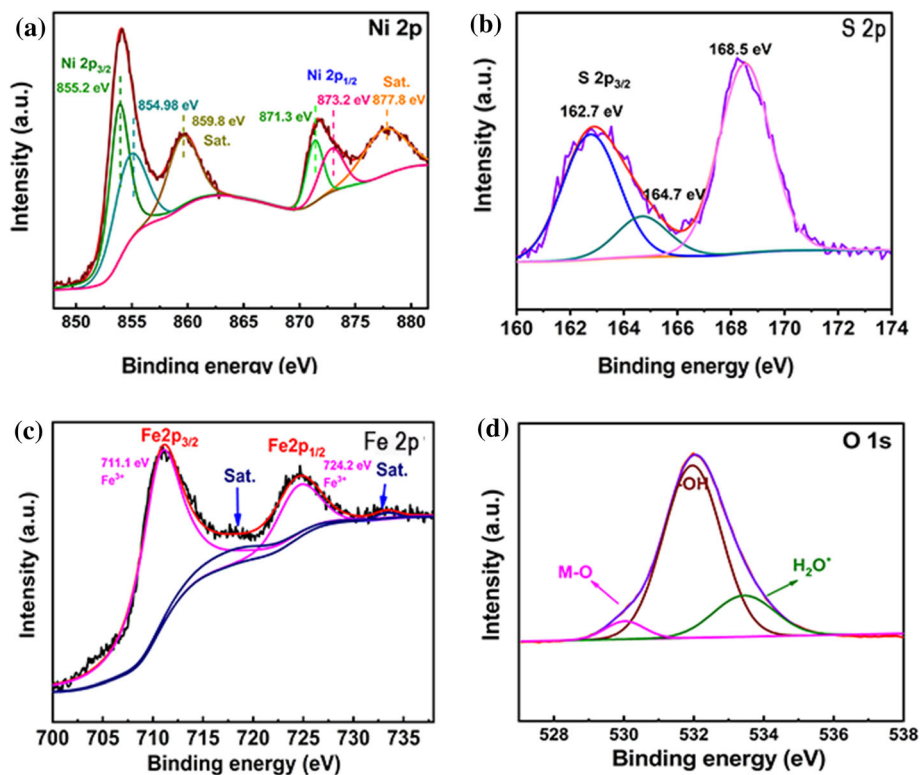
appeared at 853.4 (Ni^{2+}) and 854.8 eV (Ni^{3+}); Ni 2p$_{1/2}$ peaks located at 870.8 (Ni^{2+}), and 872.6 eV (Ni^{3+})), which is caused by the interaction of hydroxide of iron with nickel sulfide [41, 42]. Moreover, in S 2p spectrum (Fig. 3b), the binding peaks displayed at 162.7 and 164.7 eV are corresponding to Ni-S bonding structure [24, 38–40, 43]. Meanwhile, the peak at about 168.5 eV belongs to the sulfate species on account of surface oxidation [24, 44].

According to the high-resolution XPS spectra of Fe 2p (Fig. 3c), the binding energies of the fitting peaks at 711.1 and 724.2 eV are corresponding to Fe $2p_{3/2}$ and Fe $2p_{1/2}$ regions, respectively, which confirmed that Fe^{3+} plays a dominant role in the catalyst [45–47]. As for the O 1 s spectrum, three peaks (Fig. 3d) occur mainly in three areas are related to hydroxyl groups (531.7 eV), lattice oxygen (530.3 eV) and surface-adsorbed water molecules (553.5 eV) [44, 48, 49]. Among them, OH group is the main component, and a small amounts of lattice oxygen may form as a result of surface oxidation of iron substances when exposed to air.

The microstructure and composition of as-synthesized samples were further characterized by TEM. As shown in Fig. 4a and 4c, both the precursor and the final sample are composed of ultra-thin nanosheets, which is equivalent to that of the second deposition process. Moreover, the HRTEM image (Fig. 4b) of the precursor nanoarrays matches the (043) crystal plane of Ni_9S_8 with a lattice spacing of 0.213 nm. As for the nanosheets after the second deposition, it can be seen that not only the (043) plane of the precursor still exists from Fig. 4d, but also the (400) crystal plane (0.208 nm) of $Fe(OH)_3$ is generated, which further

proves that the existence of hydroxide of iron and the nickel sulfide in the composite. Therefore, after analyzing the characterization results of SEM, XRD, XPS and TEM, we conclude that the composition of the nanoarray is a composite of Ni_9S_8 and $Fe(OH)_3$.

Electrochemical performances of $Fe(OH)_3/Ni_9S_8/ESS$

Electrochemical performance tests were performed on an electrochemical workstation in 1.0 M alkaline solution (KOH). Figure 5a shows the LSV curve of stainless steel in various processes and RuO_2/ESS as the reference group. It can be seen from Fig. 5a and Fig. 5c that the first deposited vertical nanoarrays have shown excellent electrochemical properties compared to the original substrate (η_{10} = 416 mV), etched substrate (η_{10} = 350 mV) and even superior to commercial RuO_2 catalyst (η_{10} = 310 mV) at a current density of 10 mA cm^{-2}. It is noticeable that the Ni_9S_8/ESS displays a weak oxidation peak around 1.39 V (vs RHE) due to the transformation Ni(II) to Ni(III) [50, 51]. After the second electrochemical deposition, the overpotential (η) of $Fe(OH)_3/Ni_9S_8/ESS$ at 10 mA cm^{-2} decreased by 88 mV compared to

Fig. 4 a TEM image of Ni_9S_8/ESS. b HRTEM image of Ni_9S_8/ESS. c TEM image of $Fe(OH)_3/Ni_9S_8/ESS$. d HRTEM image of $Fe(OH)_3/Ni_9S_8/ESS$.
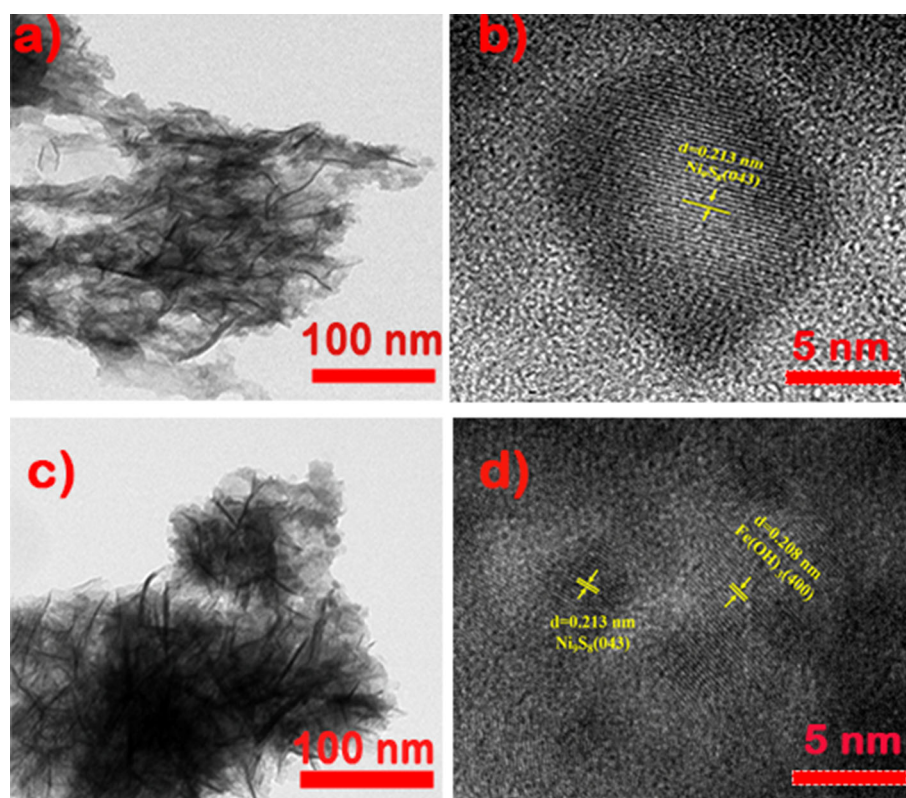
Figure 5 **a** OER polarization curves of Fe(OH)$_3$/Ni$_9$S$_8$/ESS, Ni$_9$S$_8$/ESS, RuO$_2$/ESS, ESS, and bare SS. **b** Tafel plots for the OER, and **c** Tafel slopes and overpotentials of Fe(OH)$_3$/Ni$_9$S$_8$/ESS, Ni$_9$S$_8$/ESS, RuO$_2$/ESS, ESS, and bare SS. **d** Stability test of Fe(OH)$_3$/Ni$_9$S$_8$/ESS. The inset is the LSV curve of Fe(OH)$_3$/Ni$_9$S$_8$/ESS before and after 500 CV cycles.
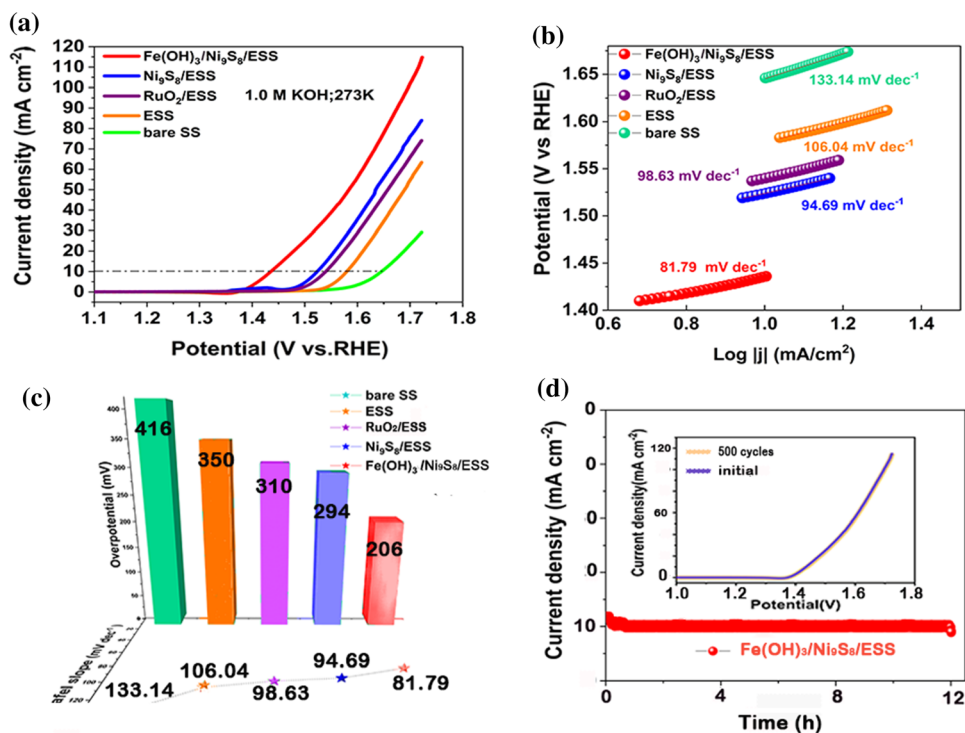

the Ni$_9$S$_8$/ESS. One of the most obvious changes is the disappearance of oxidation peaks, which is caused by the deposition of iron hydroxide on the surface of nickel sulfide. As a result, the Ni$_9$S$_8$ layer can prevent the nickel species from direct exposure to the alkaline environment and therefore does not require a higher potential to overcome the oxidation peak [36]. In addition, compared with the single Ni$_9$S$_8$ precursor and RuO$_2$, after iron deposition the current density of Fe(OH)$_3$/Ni$_9$S$_8$/ESS significantly increases to more than 100 mA cm^{-2}, making the catalyst more practical.

The OER kinetics of the catalyst was assessed using the Tafel slope. As shown in Fig. 5b, c, the as-synthesized catalyst possesses the lowest Tafel slope (81.79 mV dec^{-1}), which is lower than those of Ni$_9$S$_8$/ESS (94.69 mV dec^{-1}), ESS (106.04 mV dec^{-1}), RuO$_2$/ESS (98.63 mV dec^{-1}), and SS (133.14 mV dec^{-1}), indicating that the Fe(OH)$_3$/Ni$_9$S$_8$/ESS displayed the fastest OER kinetics among the as-prepared samples. For a practical catalyst, stability is a non-negligible property. Herein, we did 500 cycles CV scan and then we conducted a LSV test, and the obtained curve was almost the same as the curve that obtained after the first scan (the inset of Fig. 5d), which confirm its durability. Then, we performed a stability test with chronopotentiometry (CP)

near 10 mA cm^{-2}, and Fig. 5d shows that the current did not begin to decay even after 12 h, that signifies the long-term OER performance of the catalyst. Moreover, the morphology of Fe(OH)$_3$/Ni$_9$S$_8$/ESS after long-term OER process was further carried out by SEM measurement. As shown in Fig.S6, the Fe(OH)$_3$/Ni$_9$S$_8$/ESS still maintain the previous ultrathin nanosheets structure, which indicates its good structure stability in the OER process. To further study the charge transfer process at the interface of Fe(OH)$_3$/Ni$_9$S$_8$/ESS nanoarray electrode, we used EIS to conduct impedance test. According to Fig. 6a (Table S1), the fitting semicircle diameter decreases from small to large in the following order; Fe(OH)$_3$/Ni$_9$S$_8$/ESS (1.769 Ω) < Ni$_9$S$_8$/ESS (1.795 Ω) < ESS (1.81 Ω) < SS (1.88 Ω), which demonstrates the small interface resistance and fast kinetics of the Fe(OH)$_3$/Ni$_9$S$_8$/ESS. Meanwhile, the magnitude of charge transfer resistance (R$_{ct}$) also accords with this order, Fe(OH)$_3$/Ni$_9$S$_8$/ESS (2.169 Ω) < Ni$_9$S$_8$/ESS (2.543 Ω) < ESS (6.86 Ω) < SS (50.51 Ω), indicating that the catalyst of final deposition has better charge transfer properties. From the LSV curve and the Tafel slope, the prepared catalyst has excellent performance and fast kinetics toward OER. As an index to estimate the available active sites of the electrocatalyst, a double-layer capacitance based on the electrochemical active

Figure 6 a Electrochemical impedance spectroscopy and **b** double-layer capacitance (C_{dl}) data of electrocatalysts fabricated in this study.
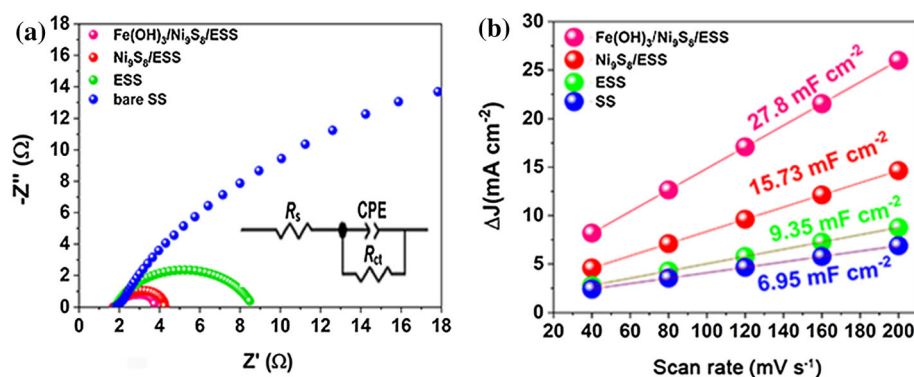
surface area was calculated [52, 53] through CV plots (Fig. S3) in the non-Faradaic potential area (0.953–1.053 V vs. RHE) at different scan rates. As expected, (Fig. 6b), $Fe(OH)_3/Ni_9S_8/ESS$ has the highest C_{dl} value, indicating that it possesses the most active sites compared to the other reference samples.

Conclusion

In summary, $Fe(OH)_3/Ni_9S_8/ESS$ nanoarrays were synthesized by electrodeposition of $Fe(OH)_3$ on a Ni_9S_8 nanoarrays precursor using a template-mediated strategy. Benefited from the nanoarrays morphology superiority and the coupling effect of $Fe(OH)_3$ and Ni_9S_8, as-constructed catalyst exhibits excellent performance than those of Ni_9S_8/ESS, RuO_2/ESS and most non-noble metal catalysts-fabricated on current collectors (Table S2) toward OER in 1.0 M alkaline electrolyte. In particular, the superior performance was ascribed to the enhanced electron transfer and abundant active sites exposure of nanoarrays architecture constructed on ESS. Moreover, the layer-by-layer electrodeposited strategy was expected to prevent the oxidation of active Ni_9S_8 during the water oxidation, and hence resulted in an exceptional long-term OER ability in a 12 h continuous *i-t* test without any current density decay. This work provides a facile synthesis strategy with novel structural design for the development of efficient and low-cost electrocatalysts.

Acknowledgements

Declarations

Conflict of interest The authors declare that they have no known competing financial interests or personal relationships that could have appeared to influence the work reported in this paper.

References

[1] Robinson M, Shine T (2018) Achieving a climate justice pathway to 1.5 °C. Nature Clim Change. 8(7):564–569. h ttps://doi.org/10.1038/s41558-018-0189-7

[2] Holden PB, Edwards NR, Ridgwell A, Wilkinson RD, Fraedrich K, Lunkeit F, Pollitt H, Mercure JF, Salas P, Lam A, Knobloch F, Chewpreecha U, Viñuales JE (2018) Climate–carbon cycle uncertainties and the Paris Agreement. Nat Clim Chang 8(7):609–613. https://doi.org/10.1038/s41 558-018-0197-7

[3] Nai J, Lu Y, Yu L, Wang X, Lou XWD (2017) Formation of Ni-Fe mixed diselenide nanocages as a superior oxygen evolution electrocatalyst. Adv Mater 29(41):1703870. http s://doi.org/10.1002/adma.201703870

[4] Li FL, Shao Q, Huang X, Lang JP (2018) Nanoscale trimetallic metal-organic frameworks enable efficient oxygen evolution electrocatalysis. Angew Chem Int Ed Engl 57(7):1888–1892. https://doi.org/10.1002/anie.201711376

[5] Lee Y, Suntivich J, May KJ, Perry EE, Shao-Horn Y (2012) Synthesis and activities of rutile IrO2 and RuO2 nanoparticles for oxygen evolution in acid and alkaline solutions. J Phys Chem Lett 3(3):399–404. https://doi.org/10.1021/jz2016507

[6] Tan Y, Wang H, Liu P, Cheng C, Zhu F, Hirata A, Chen M (2016) 3D Nanoporous metal phosphides toward high-efficiency electrochemical hydrogen production. Adv Mater 28(15):2951–2955. https://doi.org/10.1002/adma.201505875

[7] Zhang H, Maijenburg AW, Li X, Schweizer SL, Wehrspohn RB (2020) Bifunctional heterostructured transition metal phosphides for efficient electrochemical water splitting. Adv Funct Mat 30(34):2003261. https://doi.org/10.1002/adfm.202003261

[8] Sun M, Liu H, Qu J, Li J (2016) Earth-rich transition metal phosphide for energy conversion and storage. Adv Energy Mat 6(13):1600087. https://doi.org/10.1002/aenm.201600087

[9] Xiao C, Zhang B, Li D (2017) Partial-sacrificial-template synthesis of Fe/Ni phosphides on Ni foam: a strongly stabilized and efficient catalyst for electrochemical water splitting. Electrochim Acta 242:260–267. https://doi.org/10.1016/j.electacta.2017.05.015

[10] Xu J, Li J, Xiong D, Zhang B, Liu Y, Wu KH, Amorim I, Li W, Liu L (2018) Trends in activity for the oxygen evolution reaction on transition metal (M = Fe Co, Ni) phosphide pre-catalysts. Chem Sci 9(14):3470–3476. https://doi.org/10.1039/c7sc05033j

[11] Zhang R, Liu H, Wang C, Wang L, Yang Y, Guo Y (2020) Electroless plating of transition metal boride with high boron content as superior HER electrocatalyst. ChemCatChem 12(11):3068–3075. https://doi.org/10.1002/cctc.202000315

[12] Mao H, Guo X, Fu Y, Yang H, Zhang Y, Zhang R, Song X-M (2020) Enhanced electrolytic oxygen evolution by the synergistic effects of trimetallic FeCoNi boride oxides immobilized on polypyrrole/reduced graphene oxide. J Mat Chem A 8(4):1821–1828. https://doi.org/10.1039/c9ta10756h

[13] Shao Z, Qi H, Wang X, Sun J, Guo N, Huang K, Wang Q (2019) Boosting oxygen evolution by surface nitrogen doping and oxygen vacancies in hierarchical NiCo/NiCoP hybrid nanocomposite. Electrochim Acta 296:259–267. https://doi.org/10.1016/j.electacta.2018.11.006

[14] Wang ZL, Hao XF, Jiang Z, Sun XP, Xu D, Wang J, Zhong HX, Meng FL, Zhang XB (2015) C and N hybrid coordination derived Co-C-N complex as a highly efficient electrocatalyst for hydrogen evolution reaction. J Am Chem Soc 137(48):15070–15073. https://doi.org/10.1021/jacs.5b09021

[15] Zhu Y, Chen G, Xu X, Yang G, Liu M, Shao Z (2017) Enhancing electrocatalytic activity for hydrogen evolution by strongly coupled molybdenum nitride@nitrogen-doped carbon porous nano-octahedrons. ACS Catal 7(5):3540–3547. https://doi.org/10.1021/acscatal.7b00120

[16] Abghoui Y, Skúlason E (2017) Hydrogen evolution reaction catalyzed by transition-metal nitrides. J Phys Chem C 121(43):24036–24045. https://doi.org/10.1021/acs.jpcc.7b06811

[17] Ding J, Wang P, Ji S, Wang H, Brett DJL, Wang R (2019) Mesoporous nickel selenide N-doped carbon as a robust electrocatalyst for overall water splitting. Electrochim Acta 300:93–101. https://doi.org/10.1016/j.electacta.2019.01.093

[18] Yu B, Hu Y, Qi F, Wang X, Zheng B, Liu K, Zhang W, Li Y, Chen Y (2017) Nanocrystalline Ni 0.85 Se as efficient non-noble-metal electrocatalyst for hydrogen evolution reaction. Electrochim Acta 242:25–30. https://doi.org/10.1016/j.electacta.2017.05.001

[19] Zhou H, Yu F, Liu Y, Sun J, Zhu Z, He R, Bao J, Goddard WA, Chen S, Ren Z (2017) Outstanding hydrogen evolution reaction catalyzed by porous nickel diselenide electrocatalysts. Energy Environ Sci 10(6):1487–1492. https://doi.org/10.1039/c7ee00802c

[20] Zhu J, Ni Y (2018) Phase-controlled synthesis and the phase-dependent HER and OER performances of nickel selenide nanosheets prepared by an electrochemical deposition route. CrystEngComm 20(24):3344–3352. https://doi.org/10.1039/c8ce00381e

[21] Gu C, Hu S, Zheng X, Gao MR, Zheng YR, Shi L, Gao Q, Zheng X, Chu W, Yao HB, Zhu J, Yu SH (2018) Synthesis of Sub-2 nm iron-doped NiSe2 nanowires and their surface-confined oxidation for oxygen evolution catalysis. Angew Chem Int Ed Engl 57(15):4020–4024. https://doi.org/10.1002/anie.201800883

[22] Liang S, Jing M, Pervaiz E, Guo H, Thomas T, Song W, Xu J, Saad A, Wang J, Shen H, Liu J, Yang M (2020) Nickel-iron nitride-nickel sulfide composites for oxygen evolution electrocatalysis. ACS Appl Mater Interfaces 12(37):41464–41470. https://doi.org/10.1021/acsami.0c11324

[23] Yao M, Hu H, Wang N, Hu W, Komarneni S (2020) Quaternary (Fe/Ni)(P/S) mesoporous nanorods templated on stainless steel mesh lead to stable oxygen evolution reaction for over two months. J Colloid Interface Sci 561:576–584. https://doi.org/10.1016/j.jcis.2019.11.032

[24] Jiang J, Lu S, Gao H, Zhang X, Yu H-Q (2016) Ternary FeNiS2 ultrathin nanosheets as an electrocatalyst for both oxygen evolution and reduction reactions. Nano Energy 27:526–534. https://doi.org/10.1016/j.nanoen.2016.07.032

[25] Hao Z, Wei P, Kang H, Yang Y, Li J, Chen X, Guo D, Liu L (2019) Three-dimensional Fe3S4@NiS hollow nanospheres as efficient electrocatalysts for oxygen evolution reaction.

J Electroanal Chem 850:113436. https://doi.org/10.1016/j.je lechem.2019.113436

[26] Niu H-J, Wang A-J, Zhang L, Guo J-J, Feng J-J (2019) Ultrafine NiCoP-decorated N, S, P-codoped hierarchical porous carbon nanosheets as an efficient bifunctional electrocatalyst for oxygen reduction and oxygen evolution. Mat Chem Front 3(9):1849–1858. https://doi.org/10.1039/c 9qm00385a

[27] Zhang D, Mou H, Lu F, Song C, Wang D (2019) A novel strategy for 2D/2D NiS/graphene heterostructures as efficient bifunctional electrocatalysts for overall water splitting. Appl Catal B 254:471–478. https://doi.org/10.1016/j.apcatb.2019. 05.029

[28] Chen JS, Ren J, Shalom M, Fellinger T, Antonietti M (2016) Stainless steel mesh-supported NiS nanosheet array as highly efficient catalyst for oxygen evolution reaction. ACS Appl Mater Interfaces 8(8):5509–5516. https://doi.org/10.1021/ac sami.5b10099

[29] Seh ZW, Kibsgaard J, Dickens CF, Chorkendorff I, Norskov JK, Jaramillo TF (2017) Combining theory and experiment in electrocatalysis: insights into materials design. Science 355(6321):eaad4998. https://doi.org/10.1126/science.aad 4998

[30] Hu C, Zhang L, Zhao ZJ, Li A, Chang X, Gong J (2018) Synergism of geometric construction and electronic regulation: 3D Se-(NiCo)Sx /(OH)x nanosheets for highly efficient overall water splitting. Adv Mater 30(12):e1705538. http s://doi.org/10.1002/adma.201705538

[31] Mohanty B, Ghorbani-Asl M, Kretschmer S, Ghosh A, Guha P, Panda SK, Jena B, Krasheninnikov AV, Jena BK (2018) MoS2 quantum dots as efficient catalyst materials for the oxygen evolution reaction. ACS Catal 8(3):1683–1689. h ttps://doi.org/10.1021/acscatal.7b03180

[32] Dai K, Gao X, Yin L, Feng Y, Zhou X, Zhao Y, Zhang B (2019) Bifunctional self-assembled Ni0.7Co0.3P nanoflowers for efficient electrochemical water splitting in alkaline media. Appl Surf Sci 494:22–28. https://doi.org/10.1016/j.a psusc.2019.07.160

[33] Hou J, Wu Y, Zhang B, Cao S, Li Z, Sun L (2019) Rational design of nanoarray architectures for electrocatalytic water splitting. Adv Funct Mat 29(20):1808367. https://doi.org/10. 1002/adfm.201808367

[34] Bai Y, Zhang LC, Li Q, Wu Y, Wang Y, Xu M, Bao SJ (2021) Self-supported CdP2–CDs–CoP for high-performance OER catalysts. ACS Sustainable Chem Eng 9(3):1297–1303. https://doi.org/10.1021/acssuschemeng.0c 07700

[35] Du X, Yang Z, Li Y, Gong Y, Zhao M (2018) Controlled synthesis of Ni(OH)2/Ni3S2hybrid nanosheet arrays as highly active and stable electrocatalysts for water splitting.

[36] Shang X, Yan K-L, Lu S-S, Dong B, Gao W-K, Chi J-Q, Liu Z-Z, Chai Y-M, Liu C-G (2017) Controlling electrodeposited ultrathin amorphous Fe hydroxides film on V-doped nickel sulfide nanowires as efficient electrocatalyst for water oxidation. J Power Sources 363:44–53. https://doi.org/10.1016/ j.jpowsour.2017.07.056

[37] Liu J, Wang J, Zhang B, Ruan Y, Lv L, Ji X, Xu K, Miao L, Jiang J (2017) Hierarchical NiCo2S4@NiFe LDH heterostructures supported on nickel foam for enhanced overall-water-splitting activity. ACS Appl Mater Interfaces 9(18):15364–15372. https://doi.org/10.1021/acsami.7b 00019

[38] Yang H, Wang C, Zhang Y, Wang Q (2018) Chemical valence-dependent electrocatalytic activity for oxygen evolution reaction: a case of nickel sulfides hybridized with N and S co-doped carbon nanoparticles. Small 14(8):1703273. https://doi.org/10.1002/smll.201703273

[39] Ma X, Zhang X-Y, Yang M, Xie J-Y, Lv R-Q, Chai Y-M, Dong B (2021) High-pressure microwave-assisted synthesis of WSx/Ni9S8/NF hetero-catalyst for efficient oxygen evolution reaction. Rare Met 40(5):1048–1055. https://doi.org/ 10.1007/s12598-020-01704-x

[40] Khalil A, Liu Q, Muhammad Z, Habib M, Khan R, He Q, Fang Q, Masood HT, Rehman ZU, Xiang T, Wu CQ, Song L (2017) Synthesis of Ni9S8/MoS2 heterocatalyst for enhanced hydrogen evolution reaction. Langmuir 33(21):5148–5153. https://doi.org/10.1021/acs.langmuir.7b 00694

[41] Yang Y, Kang Y, Zhao H, Dai X, Cui M, Luan X, Zhang X, Nie F, Ren Z, Song W (2020) An interfacial electron transfer on tetrahedral NiS2 /NiSe2 heterocages with dual-phase synergy for efficiently triggering the oxygen evolution reaction. Small 16(1):e1905083. https://doi.org/10.1002/smI l.201905083

[42] Shao D, Li P, Zhang R, Zhao C, Wang D, Zhao C (2019) One-step preparation of Fe-doped Ni3S2/rGO@NF electrode and its superior OER performances. Int J Hydrogen Energy 44(5):2664–2674. https://doi.org/10.1016/j.ijhydene.2018.1 1.054

[43] Ren J-T, Chen L, Yuan G-G, Weng C-C, Yuan Z-Y (2019) Monolithic NixMy (M = OH, P, S, Se) nanosheets as efficient and stable electrocatalysts for overall water splitting. Electrochim Acta 295:148–156. https://doi.org/10.1016/j.el ectacta.2018.10.136

[44] Zhang R, Zhu Z, Lin J, Zhang K, Li N, Zhao C (2020) Hydrolysis assisted in-situ growth of 3D hierarchical FeS/ NiS/nickel foam electrode for overall water splitting.

Electrochim Acta 332:135534. https://doi.org/10.1016/j.elec
tacta.2019.135534

[45] Zhang T, Zhao Y, Kang S, Li Y, Zhang Q (2019) Formation of active Fe(OH)3 in situ for enhancing arsenic removal from water by the oxidation of Fe(II) in air with the presence of CaCO3. J Clean Prod 227:1–9. https://doi.org/10.1016/j.jc
lepro.2019.04.199

[46] Ma Y, Lu Z, Li S, Wu J, Wang J, Du Y, Sun J, Xu P (2020) In situ growth of amorphous Fe(OH)3 on nickel nitrate hydroxide nanoarrays for enhanced electrocatalytic oxygen evolution. ACS Appl Mater Interfaces 12(11):12668–12676. https://doi.org/10.1021/acsami.9b19437

[47] Grosvenor AP, Kobe BA, Biesinger MC, McIntyre NS (2004) Investigation of multiplet splitting of Fe 2p XPS spectra and bonding in iron compounds. Surf Interface Anal 36(12):1564–1574. https://doi.org/10.1002/sia.1984

[48] Barreca D, Carraro G, Gasparotto A, Maccato C, Warwick MEA, Kaunisto K, Sada C, Turner S, Gönüllü Y, Ruoko T-P, Borgese L, Bontempi E, Van Tendeloo G, Lemmetyinen H, Mathur S (2015) Fe2O3-TiO2 nano-heterostructure pho-
toanodes for highly efficient solar water oxidation. Adv Mat Interfaces 2(17):1500313. https://doi.org/10.1002/admi.
201500313

[49] Wang J, Teng X, Niu Y, Guo L, Kong J, He X, Chen Z (2019) In situ autologous growth of self-supporting NiFe-
based nanosheets on nickel foam as an efficient

electrocatalyst for the oxygen evolution reaction. RSC Adv 9(38):21679–21684. https://doi.org/10.1039/c9ra04368c

[50] Chen S, Kang Z, Hu X, Zhang X, Wang H, Xie J, Zheng X, Yan W, Pan B, Xie Y (2017) Delocalized spin states in 2D atomic layers realizing enhanced electrocatalytic oxygen evolution. Adv Mater 29(30):1701687. https://doi.org/10.10
02/adma.201701687

[51] Jin Y, Huang S, Yue X, Du H, Shen PK (2018) Mo- and Fe-
modified Ni(OH)2/NiOOH nanosheets as highly active and stable electrocatalysts for oxygen evolution reaction. ACS Catal 8(3):2359–2363. https://doi.org/10.1021/acscatal.7b
04226

[52] Xia C, Liang H, Zhu J, Schwingenschlögl U, Alshareef HN (2017) Active edge sites engineering in nickel cobalt sele-
nide solid solutions for highly efficient hydrogen evolution. Adv Energy Mat 7(9):1602089. https://doi.org/10.1002/aen
m.201602089

[53] Liang H, Li L, Meng F, Dang L, Zhuo J, Forticaux A, Wang Z, Jin S (2015) Porous two-dimensional nanosheets con-
verted from layered double hydroxides and their applications in electrocatalytic water splitting. Chem Mater 27(16):5702–5711. https://doi.org/10.1021/acs.chemmater.5
b02177